Ocean Chlorofluorocarbon and Heat Uptake

During the 20th Century in the CCSM3

by

Peter R. Gent,   Frank O. Bryan,   Gokhan Danabasoglu,   Keith Lindsay

National Center for Atmospheric Research
Boulder, Colorado

Daisuke Tsumune

Central Research Institute of Electric Power Industry
Chiba, Japan

Matthew W. Hecht

Los Alamos National Laboratory
Los Alamos, New Mexico

Scott C. Doney

Woods Hole Oceanographic Institution
Woods Hole, Massachusetts

Abstract

An ensemble of nine simulations for the climate of the 20th Century has been run using the Community Climate System Model version 3. Three of these runs also simulate the uptake of chlorofluorocarbon (CFC-11) into the ocean using the protocol from the Ocean Carbon Model Intercomparison Project. Comparison with ocean observations taken between 1980 and 2000 shows that the global CFC-11 uptake is simulated very well. However, there are regional biases, and these are used to identify where too much deep water formation is occuring in the CCSM3. The variability between the three runs simulating CFC-11 uptake is also briefly documented.

The variability in ocean heat content in the 1870 Control runs is shown to be only a little smaller than a recent estimate using ocean observations. The ocean heat uptake between 1957 and 1996 in the ensemble is compared to the recent observational estimates of the secular trend. The trend in ocean heat uptake is considerably larger than the natural variability in the 1870 Control runs. The heat uptake down to 300 m between 1957 and 1996 varies by a factor of two across the ensemble. Some possible reasons for this large spread are discussed. There is much less spread in the heat uptake down to 3 km. On average, the CCSM3 20th Century ensemble runs take up somewhat more heat than the recent estimate from observations. One possible explanation for this is that the CCSM3 climate sensitivity of 2.67°C is somewhat too large.

1. Introduction

What is required of a good ocean component for climate models? The first requirement is that the model produce a realistic sea surface temperature (SST) distribution, given accurate atmospheric forcing. This is necessary if the model's climate is to be realistic and stable. However, another very important requirement is to get the rate of ocean heat uptake correct. This is the primary way in which the ocean affects the transient climate response of the fully coupled model, see Raper et al. (2002). A third requirement is to get the correct rate of ocean carbon dioxide uptake, because this affects the amount of carbon dioxide that remains in the atmosphere. These requirements necessitate a very good representation of ocean mixed layer depths, ventilation of the main thermocline, and of the global meridional overturning circulation, see Doney et al. (2004).

One method of assessing an ocean component is to evaluate the ventilation rate of the thermocline and deep ocean in simulations of the 20th Century. An ensemble of nine of these simulations from 1870–2000 have been made with the Community Climate System Model version 3 (CCSM3). These use the best estimates of solar, aerosol and greenhouse gas forcing variations over the 20th Century, which are documented in Meehl et al. (2005). In order to validate CCSM3, results from the ocean component can be compared to ocean observations from the second half of the 20th Century. Three members of the ensemble, and an ocean alone simulation forced by atmospheric observations, include chlorofluorocarbon-11 (CFC-11) as a passive tracer. Ocean heat uptake in the entire ensemble will also be studied. We will compare the magnitude of climate change signals in heat content relative to the internal variability of the coupled model.

CFC-11 started to be released into the atmosphere in the 1930s. However, significant concentrations in the atmosphere and ocean did not occur until the 1950s. A large number of CFC observations were made during the World Ocean Circulation Experiment (WOCE) in all basins, concentrated in the 1991–1997 period. Enough observations have been made that global, gridded data sets are now available, along with a total ocean inventory for 1991–1997, see Willey et al. (2004). CFC-11 is a purely passive ocean tracer, and is extremely useful in evaluating thermocline ventilation rates and deep water formation sites in ocean models. In fact, the Ocean Carbon Model Intercomparison Project (OCMIP) specifically used CFC-11 to intercompare 13 global ocean models, see Dutay et al. (2002). Many of these were used as components of climate models, including the low resolution ocean component of the Climate System Model, version 1 (CSM1). The CSM1 results from an ocean alone run forced by atmospheric observations are discussed much more fully in Doney and Hecht (2002). They showed a large sensitivity of Antarctic bottom water formation to the surface forcing used, and how incorporation of ocean physical parameterizations, such as a bottom boundary layer scheme, can improve the deep ocean uptake of CFC-11 around Antarctica. CFC-11 was not included in any coupled runs of the

CSM1 and CCSM version 2, but has been included in three of the CCSM3 20th Century integrations.

Levitus et al. (2000) estimated long-term secular trends in ocean heat content from observations, and showed that the ocean had taken up heat between the 1950s and 1990s, with a significant increase in the average temperature of the upper 300 m. Several climate groups have analyzed their 20th Century runs to compare with these observations, and all have concluded that there is only a small probability that the increase is due to natural variability. Gent and Danabasoglu (2004) analyzed control and 1% per year increasing carbon dioxide coupled runs using the CCSM2, and reached the same conclusion. We will compare ocean heat uptake results from the ensemble of CCSM3 20th Century runs to the recently updated Levitus et al. (2005) estimates, and make inferences about the model internal variability and climate sensitivity.

The layout of the paper is as follows. The ocean component and CCSM3 coupled experiments will be briefly documented in Section 2. The comparisons of CFC-11 and heat uptake with ocean observations are in Sections 3 and 4, respectively. Section 5 contains our discussion and conclusions.

2. The Ocean Component and Experiments

The ocean component uses spherical coordinates in the southern hemisphere, but in the northern hemisphere the pole is displaced into Greenland at 80°N, 40°W. The horizontal grid has 320 (zonal) × 384 (meridional) grid points, and the resolution is uniform in the zonal, but not in the meridional, direction. In the southern hemisphere, the meridional resolution is 0.27° at the equator, gradually increasing to 0.54° at 33°S, and is constant at higher latitudes. There are 40 levels in the vertical, whose thickness increases from 10 m near the surface to 250 m in the deep ocean. The minimum and maximum depths are 30 m and 5.5 km. The domain is global, which includes Hudson Bay, the Mediterranean Sea, and the Persian Gulf. The time step used is one hour, which is small enough that no Fourier filtering is required around the displaced Greenland pole.

The horizontal viscosity is a Laplacian operator that is anisotropic following the formulation of Smith and McWilliams (2003), and uses different coefficients in the east-west and north-south directions. The vertical mixing scheme is the K-profile parameterization (KPP) scheme of Large et al. (1994). A change in the KPP numerical implementation, compared to the CCSM2, has resulted in deeper, more realistic ocean mixed layer depths. The parameterization of the effects of mesoscale eddies is that of Gent and McWilliams (1990). Further details of the CCSM3 ocean component can be found in Danabasoglu et al. (2005) and Smith and Gent (2004).

The implementation of the CFCs follows the OCMIP-2 protocols, see Section 3 of Dutay et al. (2002), except that surface wind speed, atmospheric pressure, and ice fraction

4

are from the atmosphere and sea ice components, and not from the specified protocols. However, there was an error in the implementation of the transition between the northern and southern hemisphere atmospheric CFC partial pressure (pCFC). The transition was imposed over ± 10 radians instead of $\pm 10°$, so that most of the ocean saw near equatorial values of atmospheric pCFC. The hemispheric pCFC averages should differ by 10–20%, with the northern hemisphere having the larger values. This is a result of the larger northern hemisphere sources and a not very fast inter-hemispheric mixing time. Thus, while the model hemispheric oceanic CFC inventories are biased by 5–10%, the error in the global oceanic CFC inventories is much smaller, because the two hemispheric biases compensate each other quite closely. The implementation was correct in the CCSM3 ocean alone run forced by observations.

A list of all the integrations is shown in Table 1. The final configuration of the 1870 Control integration was run at NCAR (NC1870) for years 280–510. Five 20th Century integrations were run at NCAR and Oak Ridge National Laboratory, that branched from the NC1870 run at years 360, 380, 400, 420, and 440, respectively, and run for 130 years; 1870–2000. These are labelled NCa, ORb, NCc, ORd, and NCe in Table 1. Another 1870 Control integration was run at the Earth Simulator (ES1870), which branched from the NC1870 run at year 300 and continued until year 960. Four 20th Century integrations were run at the Earth Simulator, labelled ESb, ESf, ESg, and ESh, that branched from the ES1870 run at years 380, 410, 460, and 540 respectively. Runs ESb, ESg, and ESh are the three 20th Century integrations that contain simulations of CFC-11. In addition to these fully coupled runs, we show results from a CCSM3 ocean alone integration, labelled Ocn in Table 1. This run was forced by observed atmospheric fields from 1958-2000, that are documented in Large and Yeager (2004).

3. CFC-11 Results

First, qualitative comparisons with CFC-11 observations taken on particular WOCE sections in the North and South Atlantic and South Pacific will be made. These sections were chosen because they include regions where there is significant ventilation of the deep ocean. In other regions, such as the Indian and North Pacific Oceans where most of the CFC-11 has remained in the upper ocean, comparisons between the model and WOCE sections are good, which indicates that the KPP vertical mixing scheme is performing quite well. CFC solubility is a strong function of temperature, so that the data–model comparison of CFC-11 concentrations will reflect both the temperature structure and ventilation pathways of the ocean. An alternative approach is to compare CFC partial pressures, but we will not do this here.

Figure 1a shows the monthly-averaged CFC-11 from na93, the August 1993 NOAA reoccupation of the WOCE a16n section along 20°W in the North Atlantic. Figures 1b

5

and 1c show the comparable plots from the Ocn run, and the mean of the ESb, ESg and ESh runs. The observations show most of the CFC-11 above 500 m in the subtropics, with surface values of about 2 pmol kg^{-1}. The surface value increases monotonically towards higher latitudes, and attains a value of about 4 pmol kg^{-1} at 62°N. The CFC has also penetrated deeper monotonically towards the north, with the 0.1 pmol kg^{-1} contour reaching 4 km depth by 50°N. Polewards of 45°N, the 1 pmol kg^{-1} value is at a depth of about 2 km. The ocean alone and coupled runs show the same general features, but there are important differences. They have too small values between 600 m and 1 km north of 45°N, and too large values between 1.5 and 2 km centered at 50°N. The error between 600 m and 1 km is probably because the model Gulf Stream is directly bringing low CFC-11 water from the south into this region, because it is too zonal across the North Atlantic. The too high values below suggest that high CFC water is being advected east of the mid-Atlantic Ridge from the western North Atlantic, instead of moving more directly southwards as part of the deep western boundary current. There is some spread across the three CFC runs, which is shown in Fig. 1d. This shows the column inventory along the section from the observations (crosses), Ocn run (squares), and the shading gives the range from the ESb, ESg and ESh runs. There is very little spread south of 40°N, but considerable spread farther north around 50°N. This is caused by the different timing of deep mixing events centered at 50°N, which penetrate through the CFC minimum at 1 km. Even so, the ensemble spread does not bracket the observations at this latitude.

Figure 2 shows the equivalent plot for the ajax section along 0° in the South Atlantic from October 1983. The observations show high values > 1 pmol kg^{-1} reaching down to 800 m in a region centered at 40°–45°S. This represents subduction of surface water down along isopycnal surfaces. There are values > 0.1 pmol kg^{-1} throughout the water column between 53° and 60°S, which is only reproduced very weakly in the Ocn run, but is much better in the 20th Century runs. This is probably due to stronger winds in the coupled runs, especially between 40° and 50°S. The Ocn run has a poor representation of the deep ocean observations, which is only improved somewhat in the coupled runs. Doney and Hecht (2002) show a similar poor representation of the deep observations along this section using the CSM1 ocean component. They traced this to insufficient westward transport of deep CFC-tagged water along the continental slope of Antarctica east of the Weddell Sea. The comparison between model results and observations was better a little further west directly north of the Weddell Sea. Figure 2d shows the ensemble spread is largest between 50° and 65°S, again where there is significant ventilation of the deep ocean, and the 20th Century runs match the observations well. The spread is much smaller between 20° and 45°S, where the CCSM3 values are significantly smaller than the observations.

Figure 3 shows results from the February 1996 WOCE p14s section near 170°E in the South Pacific. The observations show similar characteristics to the South Atlantic section, with values > 1 pmol kg^{-1} down to 1 km between 45° and 55°S and values about 0.1 pmol

6

kg^{-1} in the deep ocean, especially near Antarctica. The subduction along isopycnals is captured quite well by the Ocn and coupled runs, with the higher surface values reaching slightly deeper in the coupled runs. However, there are too high CFC-11 concentrations in the deep ocean in the model at this longitude, and again the 20th Century runs have higher values than the Ocn run. Figure 3d shows a small ensemble spread along this section, which cannot bracket the much lower observed values near Antarctica at this longitude. This clearly shows that there is too much deep water formation in the west Pacific sector near Antarctica. The most likely reason is the winds blowing off Antarctica are too strong, which blow the sea ice away from the coast too quickly. More sea ice is then formed along the coast, which rejects too much brine into the upper ocean and causes more deep convection than in the present climate. Doney and Hecht (2002) show the WOCE p15s section from the CSM1 ocean component alone run forced by observations, where there was too little deep convection at 170°W. They show a strong sensitivity of the convection strength to the salinity values used in the under-ice restoring term. In an ocean alone run, this simulates brine rejection in a fully coupled run, and the deep ocean solutions are sensitive to this restoring term.

Figures 1–3 showed comparisons of CFC-11 concentrations from a climate model simulation with measurements from a single occupation of an ocean section. Differences can arise from other sources than the one we wish to document, which is model systematic bias. The horizontal resolution of the ocean component of climate models, including the CCSM3, does not capture the variability due to mesoscale eddies. Haine and Gray (2001) and Peacock et al. (2005) document the amplitude of eddy variability in CFC-11 concentrations, which they call the "model variability error", by using a combination of simulations with eddy-resolving and non-eddy resolving models. However, in the case of historical climate simulations, there is another source of disagreement because they are not simulating the state of the climate system for particular years, but rather one of many possible realizations of the climate system for those years. We have attempted to document the amplitude of this "realization variability error" by showing the ensemble spread in Figs. 1–3, although the ensemble size of three is rather small.

In order to further document the "realization variability error", Fig. 4 shows the root-mean-square of the CFC-11 concentration at 200 m depth in the Indian Ocean relative to the ensemble mean for each month of 1995. This is calculated from 36 samples (12 months and 3 ensemble members), and is directly comparable with Fig. 7 of Peacock et al. (2005), which shows their "model variability error". We note that the "realization variability error" has a number of features in common with the "model variability error". A band of maximum variability runs east-west near 15°S, but with a smaller amplitude compared to the eddy variability shown in Peacock et al. However, the variability among the ensemble members in the Antarctic Circumpolar Current region exceeds that due to mesoscale eddies. In contrast, the ensemble has little variability in the Agulhas retroflection

7

region, where mesoscale variability is very large. Background levels of ensemble variability away from these regions is smaller than the background eddy variability in Peacock et al. Figure 12 of Peacock et al. (2005) shows vertical profiles of CFC-11 at stations along the WOCE i03 track, which document the "model variability error" is largest around 400 m depth. The amplitude of the CCSM3 two standard deviation "realization variability error" of 0.1–0.2 $\mathrm{pmol\,kg}^{-2}$ at this depth is an order of magnitude smaller than the "model variability error" due to mesoscale eddies estimated by Peacock et al.

As mentioned in the Introduction, Willey et al. (2004) have produced a column inventory of CFC-11 centered on 1994 from all the WOCE data. It is shown in Fig. 5a, with the same quantity from the Ocn run in Fig. 5b, and the mean of runs ESb, ESg and ESh in Fig. 5c. The observations show the smallest values in the tropics, especially at $10°$N in the eastern Pacific Ocean and in the very northern Indian Ocean, and the largest values in the northwest North Atlantic south of Greenland. The other band of large values follows the path of the Antarctic Circumpolar Current, and there are smaller values to the south near Antarctica. The Ocn run shows the same general features, but the maximum values are smaller, except in the North Atlantic north of $40°$N. As always with ocean alone runs, it is rather difficult to know whether the differences compared to observations are due to the forcing data used, in particular to the under ice salinity restoring, or to the physics of the ocean component. The 20th Century runs in Fig. 5c show larger regions of small values in the tropics, especially in the Pacific where the signature of thermocline depth errors associated with the double intertropical convergence zone shows up clearly. However, at higher latitudes the 20th Century run values are larger, probably as a result of stronger surface winds that produce deeper ocean mixed layers, stronger midlatitude gyres, and a deeper main thermocline. The values in the Antarctic Circumpolar Current are now slightly larger than the observations, but the large values extend to the Antarctic coast in the east Indian and west Pacific sectors. This results from the high values in the deep ocean shown in Fig. 3c along $170°$E. This is the region of the largest discrepancy between the 20th Century runs and the observations. The values in the northern North Atlantic are also too large, but are not much different than those in the Ocn run.

Another measure of CFC uptake is the penetration depth, which is defined as the column inventory divided by the surface concentration, see Dutay et al. (2002). Figure 6 shows results from observations, the Ocn run, and the 20th Century run mean in the same format as Fig. 5. In the observations, large values > 1 km occur over much of the North Atlantic, with maximum values > 2.5 km. In the North Pacific, values up to 900 m occur in the Kuroshio area. In the southern hemisphere, values > 1 km occur in the southern Indian and Atlantic Oceans, and southeast of New Zealand. This pattern is reproduced well in the Ocn run, but the penetration depths are too small, except in the northern North Atlantic. In the 20th Century runs, the penetration depth is improved in the North Atlantic, where values > 1 km are more extensive and the maximum value is

8

< 3 km, and in the southern Indian Ocean and around New Zealand, where the depths have been increased by about 200 m. The penetration depth also increased in the North Pacific, but at the southern flank of the subtropical gyre, instead of farther northwest near the Kuroshio.

Figures 5 and 6 show the mean values from the three 20th Century runs that have CFC-11. The variability in the column inventory and penetration depth is largest by far in the subpolar North Atlantic and the Labrador Sea. There is smaller variability near Antarctica between 120° and 160°E, and off the Kamchatka Peninsula. Elsewhere, the CFC-11 variability is quite small. Much of this variability is caused by the different timing of deep water formation events in these runs, especially in the North Atlantic.

Figure 7 shows the global CFC-11 inventory as a function of time from the ESb, ESg, ESh and Ocn runs. There is very little variability in the global CFC uptake rates in the 20th Century runs, and all have a global inventory of 5.8×10^8 moles in 1994. This compares very well with the Willey et al. (2004) estimate of $5.5 \pm 1.2 \times 10^8$ moles. This very good agreement is not affected by the implementation error described in Section 2, because its effect on the global CFC-11 inventory is almost certainly much smaller than the observational error bar of $\pm 20\%$. As discussed above, the Ocn run shows a somewhat smaller global uptake of CFC-11, with a 1994 value just above the lower bound of the estimate based on WOCE observations.

4. Heat Uptake Results

Levitus et al. (2005) have recently completed a new analysis of heat content changes between 1955 and 2003 over two depth ranges down to 300 and 700 m, and from 1955–1959 to 1994–1998 for the heat content down to 3 km. We will look at heat content changes over these depth ranges, in order to compare with the latest Levitus et al. observed trends. Results will be shown in terms of the annual-mean average potential temperature for each volume considered. First, this normalizes the heat content changes with respect to the varying sizes of the different ocean basins, and second the results are then in terms of familiar temperature units. The average potential temperature can be converted into heat content by multiplying by $\rho_0 c_p$ times the volume of ocean in the various domains. In the model, $\rho_0 c_p$ is constant equal to 4.1×10^6 J °C^{-1} m^{-3}.

In the ES1870 run the ocean is losing heat at the globally averaged rate of about 0.5 W m^{-2} over years 300–700. Most of this is coming from mid-depths in the ocean, but there is a non-negligible trend in the upper 300 m. To eliminate this small trend, heat content anomalies for both control runs and ensemble members are calculated by subtracting the linear least-squares fit to the ES1870 heat content time series over the period 300–700 years. The resulting time series of the upper 300 m heat content anomaly from the ES1870

9

run are shown in Fig. 8. It shows peak-to-peak decadal variability with a maximum range of $> 0.2°C$ in the Pacific Ocean, nearly $0.3°C$ in the Indian and Atlantic Oceans, and $0.1°C$ in the Global Ocean. The Indian and Atlantic Ocean values are comparable to the amplitude of decadal variability shown in Fig. S1 of Levitus et al. (2005), the Pacific Ocean value is a little smaller, and the Global Ocean value is somewhat smaller than the Levitus et al. values. A frequent criticism of coarse resolution climate models is that they severely underestimate natural variability; this is not the case for the CCSM3 ocean heat content down to 300 m.

Figure 9 shows the average temperature difference down to 300 m between the ESb, ESf, ESg and ESh runs minus the least-squares fit to the ES1870 run trend. Figure 9d shows that the 300 m Global Ocean heat content either remains nearly constant or falls somewhat over the first 13 years, but then all four runs have a sharp decline of about $0.1°C$ in 1883. This is in response to the Krakatoa volcano eruption. In fact, all the five large dips in the curves can be traced to a volcano; the last two are El Chicon in 1983 and Mount Pinatubo in 1991. The volcanic signal is also very clear in the Pacific and Indian Oceans, but considerably smaller in the Atlantic Ocean. Even so, the Atlantic loses heat for about 30 years until 1900, before gaining heat between 1900 and 2000. There is some spread in the rates of ocean heat uptake among the four ensemble members. The ESg run shows much slower heat uptake in the Pacific Ocean between 1940 and 1970, but then it increases so that the heat uptake catches the other three runs by the year 2000. The ESb run shows uniformly more heat uptake in the Indian, Atlantic and Global Oceans than the other three runs.

Figure 10 shows the average temperature difference down to 3 km in the same format as Fig. 9. Again, the five large volcano events show up clearly in the Global Ocean curves. These curves diverge somewhat after 1950, and the ESg run has a 25% larger heat uptake by 2000 than the other three runs. Figure 10c shows very interesting differences in the Atlantic Ocean. By 1970 the ESb run has the same temperature as 1870, whereas the temperature in the ESf and ESg runs has increased by $0.08°C$. However, by 2000 there are much smaller differences in the Atlantic heat content among the runs. There are also quite large differences in the Indian Ocean early in the 20th Century, and between 1980 and 2000 in the Pacific Ocean, again illustrating significant variability in the ocean circulation among the ensemble of 20th Century runs.

The Global Ocean average temperature increases between 1957 and 1996 from the 20th Century ensemble minus the least-squares fit to the ES1870 run trend are plotted in Fig. 11. Also shown are the recent estimates for 300 m, 700 m, and 3 km from Levitus et al. (2005). We should first note that the temperature increases shown are somewhat dependent upon the time interval chosen. The 300 m values would be increased by up to 15% if the time period had been extended to 2000, because the heat uptake is large over the last few years in all runs. Figure 11 shows that the 300 m temperature increase

varies by more than a factor of two across the ensemble, from 0.12 to 0.267°C. There is considerably less spread in the 700 m temperature increases, which are between 0.116 and 0.19°C, and the ensemble does not bracket the Levitus et al. estimate. This is also the case for the 3 km values, which range between 0.044 and 0.064°C. On average, the ensemble members have about 25% larger heat uptake down to 3 km between 1957 and 1996 than the Levitus et al. (2005) estimate from ocean observations.

Figure 12 shows the spatial patterns of the changes in heat content down to 300 m and 3 km between 1955-1959 and 1994-1998. Figure 12a shows that the largest region with an average temperature increase of >0.5°C over 300 m is the subpolar North Atlantic, Labrador Sea, Greenland-Iceland-Norwegian (GIN) Seas, and the Barents Sea north of Norway. There is a dipole structure in the North Pacific, with a significant cooling in the northeast Pacific centered at 40°N. There is also warming in the southern hemisphere, perhaps associated with changes in the path of the ACC. The heat uptake down to 3 km, shown in Fig. 12b, is much more spatially uniform, with most of the World Ocean warming between 0 and 0.1°C. There are some regions of heat loss, and areas of shelf seas, such as the Bering Sea, where there was a larger heat gain. However, the largest increase is again in the subpolar North Atlantic, Labrador, GIN and Barents Seas. These are associated with a retreat of the Arctic sea-ice, and perhaps changes in the thermohaline circulation. These large increases are consistent with the Levitus et al. (2005) results, because they also find the largest heat content changes in the North Atlantic. They estimate an average temperature increase over 40 years of 0.3°C down to 300 m and 0.1°C down to 3 km in the North Atlantic, which are at least 50% higher than increases in other large ocean basins.

What causes the wide spread of 300 m heat uptake rates in the 20th Century ensemble shown in Fig. 11? Figure 13a shows the standard deviation of the 300 m heat content in the 20th Century ensemble, with values >0.5°C shaded. The largest variability is in those locations where the average 300 m heat content is changing most, see Fig. 12a, plus the equatorial Pacific where there is El-Nino/Southern Oscillation variability. The largest variability is in the subpolar North Atlantic, Labrador, GIN and Barents Seas, which is linked to changes in the North Atlantic thermohaline circulation. There is large natural variability in the strength of the North Atlantic thermohaline circulation in the two 1870 Control runs, see Bryan et al. (2005). The amplitude is about ±20% of the mean maximum overturning value of 22 Sv, with a period of about 20 years. It is clear from this work that the thermohaline circulation variability strongly affects the mean and variability of both the CFC-11 uptake, see Figs. 5 and 6, and the ocean heat uptake over the 20th Century, see Figs. 12 and 13a.

Figure 13b shows the correlation between the North Atlantic meridional overturning maximum and the detrended 300 m average temperature over years 300–700 from the ES1870 control run. We compute a lag-1 autocorrelation of 0.86 from the overturning maximum timeseries, which indicates that there are about 30 independent samples in the

400 year time series, so that the 95% confidence level is 0.36. The figure shows that the North Atlantic and Arctic Ocean 300 m heat content is very highly correlated to the thermohaline circulation strength, with a significant anticorrelation in the subtropical North Atlantic. We have also calculated the correlations (not shown) between decadal averages of the ES1870 300 m heat storage and heat storage anomalies with respect to the mean of the 20th Century ensemble. These correlations are high if just the first part of the 20th Century runs is used, and decrease as more of the 20th Century runs are used in the calculations. However, the correlations remain marginally significant if they are calculated using the entire 20th Century runs. This demonstrates that the 300 m heat uptake can be influenced by the phase of the thermohaline circulation oscillation when a 20th Century run is started. The 20th Century runs started at different phases of the thermohaline circulation oscillation in the NC1870 and ES1870 runs, and this can affect the spread in 300 m heat uptake values shown in Fig. 11. The best way to create initial conditions for an ensemble of 20th Century runs is an interesting and important question, but is beyond the scope of this paper.

5. Discussion and Conclusions

The CFC-11 uptake simulations in three 20th Century runs have been compared with observations from WOCE sections, and are generally good in regions of the ocean where most of the CFC-11 remains above the thermocline. This indicates that the KPP vertical mixing scheme is performing well, and the wind driven circulation is realistic in these regions. The comparisons show differences where there is deep water formation in the North Atlantic, and in the west Pacific and Indian Ocean sectors near Antarctica. These differences cannot be explained by the spread in the three 20th Century runs. This "realization variability error", due to the fact that these runs do not simulate the climate for particular years, at 200 m depth in the Indian Ocean is shown in Fig. 4. A direct comparison with the "eddy variability error" in Peacock et al. (2005) shows that the eddy error is larger in most regions, but the realization error is larger in the Southern Ocean along the path of the Antarctic Circumpolar Current.

Comparison of the CFC-11 column inventory with the observational estimate centered on 1994 in Willey et al. (2004) shows that the CCSM3 is producing too much deep water off Antarctica in the Indian Ocean and west Pacific Ocean sectors. It also suggests the Labrador Sea deep water formation might be slightly too strong. These aspects of the CCSM3 ocean circulation need to be improved, because getting a realistic thermohaline circulation is very important in order that the CCSM3 produces realistic future climate scenarios. Despite these regional differences, Fig. 7 shows the first conclusion of this paper which is that the Global Ocean uptake of CFC-11 is captured rather well in the three 20th

Century runs. The CFC-11 uptake in the Ocn run is smaller, but is also within the error bar of the observational estimate.

Figure 8 shows the second conclusion of this paper that the CCSM3 300 m heat content variability is only a little smaller than the Levitus et al. (2005) observational estimate. There is considerable variability in how the ocean takes up heat across the 20th Century run ensemble. This variability is across all ocean basins and to all depths. However, the spread is largest in the 300 m heat uptake, where it is more than a factor of two, and reduces with depth; it is about 40% in the 3 km heat uptake. Figure 13b shows a strong correlation between the strength of the North Atlantic overturning circulation and the 300 m heat content in the ES1870 control run. Correlations between the control run heat content and the 20th Century 300 m heat content anomalies are also significant. Thus, the large spread in the 300 m heat uptake rates between 1957 and 1996 shown in Fig. 11 is not only due to the phase of the thermohaline variability in the late 20th Century, but could also be partly due to the different states of the thermohaline circulation when the 20th Century runs are initialized. The thermohaline circulation provides the inertia of the ocean system that gives long persistence timescales in upper ocean heat content.

Figure 11 shows the third conclusion of this paper that the ensemble average heat uptake between 1957 and 1996 down to 300 m, 700 m and 3 km is about 25% larger than the Levitus et al. (2005) observational estimate. The CCSM3 ocean heat uptake depends upon the veracity of the ocean component, the parameterized effects of volcanos, and the climate sensitivity, which mostly governs the atmospheric surface temperature response to imposed greenhouse gas levels. The successful CFC-11 comparison gives confidence that the CCSM3 ocean component does a good job simulating the uptake of heat into the ocean. If it is further assumed that the Levitus et al. (2005) estimate is correct, and that the volcano parameterization is perfect, then this implies that the CCSM3 climate sensitivity of $2.67°C$ is at least 25% too high. The "at least" in the previous sentence is because Raper et al. (2002) have shown that the transient response in climate models is always smaller than the equilibrium response. However, the combined error bars in the observed estimate, volcano parameterization and the ocean component heat uptake veracity are certainly larger than 25%.

Acknowledgments

References

Bryan, F. O., G. Danabasoglu, N. Nakashiki, Y. Yoshida, D. H. Kim, J. Tsutsui, and S. C. Doney, 2005: Response of the North Atlantic thermohaline circulation and ventilation to increasing carbon dioxide in CCSM3. *J. Climate*, Submitted.

Danabasoglu, G., W. G. Large, J. J. Tribbia, P. R. Gent, B. P. Briegleb, and J. C. McWilliams, 2005: Diurnal ocean-atmosphere coupling. *J. Climate*, Submitted.

Doney, S. C. and M. W. Hecht, 2002: Antarctic bottom water formation and deep-water chlorofluorocarbon distributions in a global ocean climate model. *J. Phys. Oceanogr.*, **32**, 1642–1666.

Doney, S. C., et al., 2004: Evaluating global ocean carbon models: The importance of realistic physics. *Global Biogeochem. Cycles*, **18**, GB3017, doi:10.1029/2003GB002150.

Dutay, J. C. et al., 2002: Evaluation of ocean model ventilation with CFC-11: comparison of 13 global ocean models. *Ocean Model.*, **4**, 89–120.

Gent, P. R., and G. Danabasoglu, 2004: Heat uptake and the thermohaline circulation in the Community Climate System Model, version 2. *J. Climate*, **17**, 4058– 4069.

Gent, P. R., and J. C. McWilliams, 1990: Isopycnal mixing in ocean circulation models. *J. Phys. Oceanogr.*, **20**, 150–155.

Haine, T. W. N., and S. L. Gray, 2001: Quantifying mesoscale variability in ocean transient tracer fields. *J. Geophys. Res.*, **106**, 13861–13878.

Large, W. G., J. C. McWilliams, and S. C. Doney, 1994: Oceanic vertical mixing: A review and a model with a nonlocal boundary layer parameterization. *Rev. Geophys.*, **32**, 363–403.

Large, W. G., and S. G. Yeager, 2004: Diurnal to decadal global forcing for ocean and sea-ice models: The data sets and flux climatologies. NCAR Technical Note, NCAR/TN–460+STR. Available online at http://www.cgd.ucar.edu/oce/pubs/04pubs.html.

Levitus, S., J. I. Antonov, T. P. Boyer, and C. Stephens, 2000: Warming of the world ocean. *Science*, **287**, 2225–2229.

Levitus, S., J. I. Antonov, T. P. Boyer, 2005: Warming of the world ocean, 1955–2003. *Geophys. Res. Let.*, In press.

Meehl, G. A., W. M. Washington, B. Santer, J. Arblaster, A. Hu, D. Lawrence, and H. Teng, 2005: Climate change in the 20th and 21st Centuries and climate change commitment in the CCSM3. *J. Climate*, Submitted.

Peacock, S., M. Maltrud, and R. Bleck, 2005: Putting models to the data test: a case study using Indian Ocean CFC-11 data. *Ocean Model.*, **9**, 1–22.

Raper, S. C. B., J. M. Gregory, and R. J. Stouffer, 2002: The role of climate sensitivity and ocean heat uptake on AOGCM transient temperature response. *J. Climate*, **15**, 124–130.

Smith, R. D., and P. R. Gent, 2004: Reference manual for the Parallel Ocean Program (POP): Ocean component of the Community Climate System Model (CCSM2.0 and CCSM3.0). Los Alamos National Laboratory Technical Report LA-UR-02-2484. Available online at http://www.ccsm.ucar.edu/models/ccsm3.0/pop.

Smith, R. D., and J. C. McWilliams, 2003: Anisotropic horizontal viscosity for ocean models. *Ocean Model.*, **5**, 129–156.

Willey, D. A., R. A. Fine, R. E. Sonnerup, J. L. Bullister, W. M. Smethie, and M. J. Warner, 2004: Global oceanic chlorofluorocarbon inventory. *Geophys. Res. Let.*, **31**, L01303, doi:10.1029/2003GL018816.

Label	Description	Years Run	CFCs
NC1870	1870 Control	280–510	
NCa	20th Century	360–490	
ORb	20th Century	380–510	
NCc	20th Century	400–530	
ORd	20th Century	420–550	
NCe	20th Century	440–570	
ES1870	1870 Control	300–960	
ESb	20th Century	380–510	Yes
ESf	20th Century	410–540	
ESg	20th Century	460–590	Yes
ESh	20th Century	540–670	Yes
Ocn	Ocean alone	1958–2000	Yes

Table 1. List of numerical experiments.

Figure Captions

1. CFC-11 from the na93 section along 20°W taken in August 1993. (a) Observations, (b) ocean alone Ocn run, (c) mean of the ESb, ESg and ESh runs, and (d) column inventory of CFC-11 in moles km^{-2} along the section from observations (crosses), Ocn run (squares), and the range of the ESb, ESg and ESh runs (shading).

2. Same as Fig. 1, but from the WOCE ajax section along 0°taken in October 1983.

3. Same as Fig. 1, but from the WOCE p14s section near 170°E taken in February 1996.

4. The rms of CFC-11 relative to the ensemble mean annual cycle over 1995 at 200 m depth in the Indian Ocean using the ESb, ESg and ESh runs; CI is 0.1 pmoles kg^{-1}.

5. Column inventory of CFC-11 in moles km^{-2} for 1994. (a) WOCE data from Willey et al. (2004), (b) ocean alone Ocn run, and (c) mean of ESb, ESg, and ESh runs.

6. Same as Fig. 5, but for penetration depth in m.

7. Time series of the global inventory of CFC-11 in moles from the ESb, ESg, ESh, and Ocn runs. Also plotted is the Willey et al. (2004) estimate centered on 1994.

8. Detrended time series of the 300 m average temperature anomaly in °C from the ES1870 control run. (a) Pacific Ocean, (b) Indian Ocean, (c) Atlantic Ocean, and (d) Global Ocean.

9. Time series of the 300 m average temperature difference in °C between the ESb, ESf, ESg and ESh runs minus the ES1870 control run. (a) Pacific Ocean, (b) Indian Ocean, (c) Atlantic Ocean, and (d) Global Ocean.

10. Same as Fig. 9, but for the 3 km average temperature.

11. The 300 m, 700 m and 3 km average temperature increases in °C for the Global Ocean between 1957 and 1996 from the ensemble of 20th Century runs. Also plotted are the Levitus et al. (2005) observational estimates.

12. The ensemble mean 20th Century average temperature change between 1955-1959 and 1994-1998 in °C: a) 300 m and b) 3 km.

13. a) Standard deviation of the 300 m heat content among the 20th Century ensemble; CI is 0.25°C, and b) correlation between the North Atlantic meridional overturning maximum and the 300 m heat content over years 300-700 from the ES1870 control run; CI is 0.2.
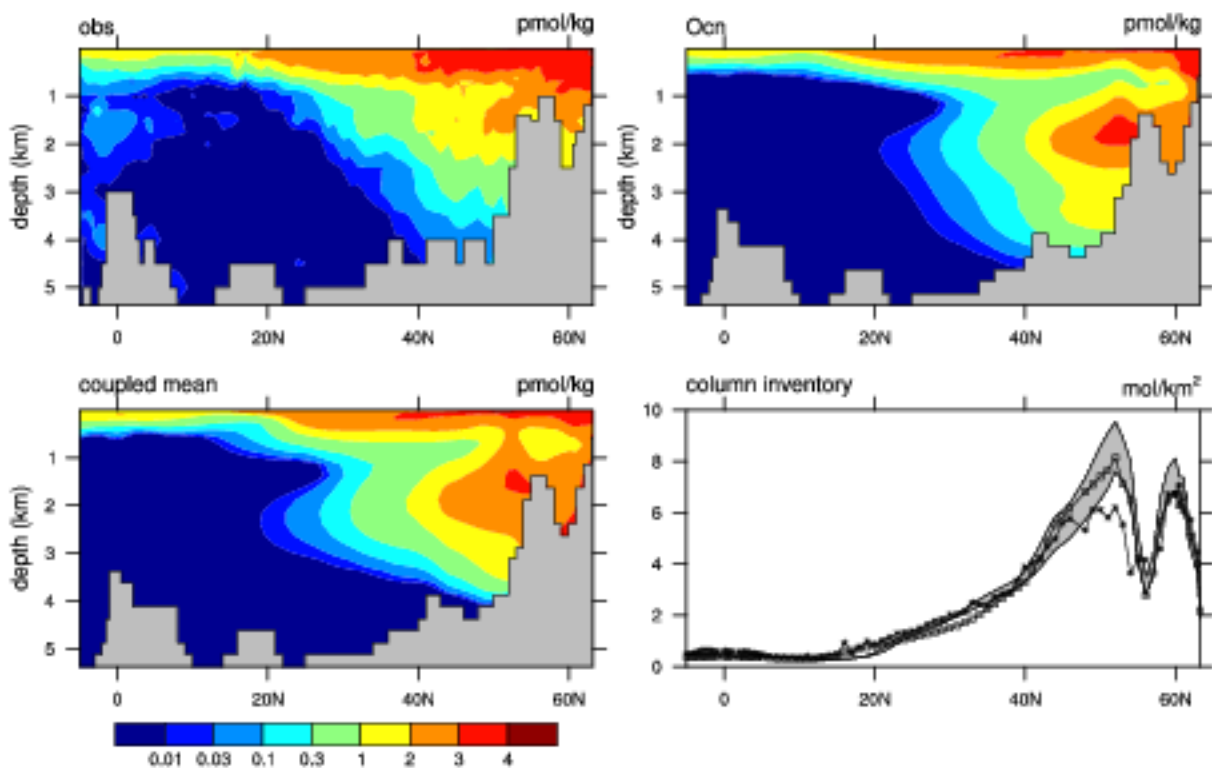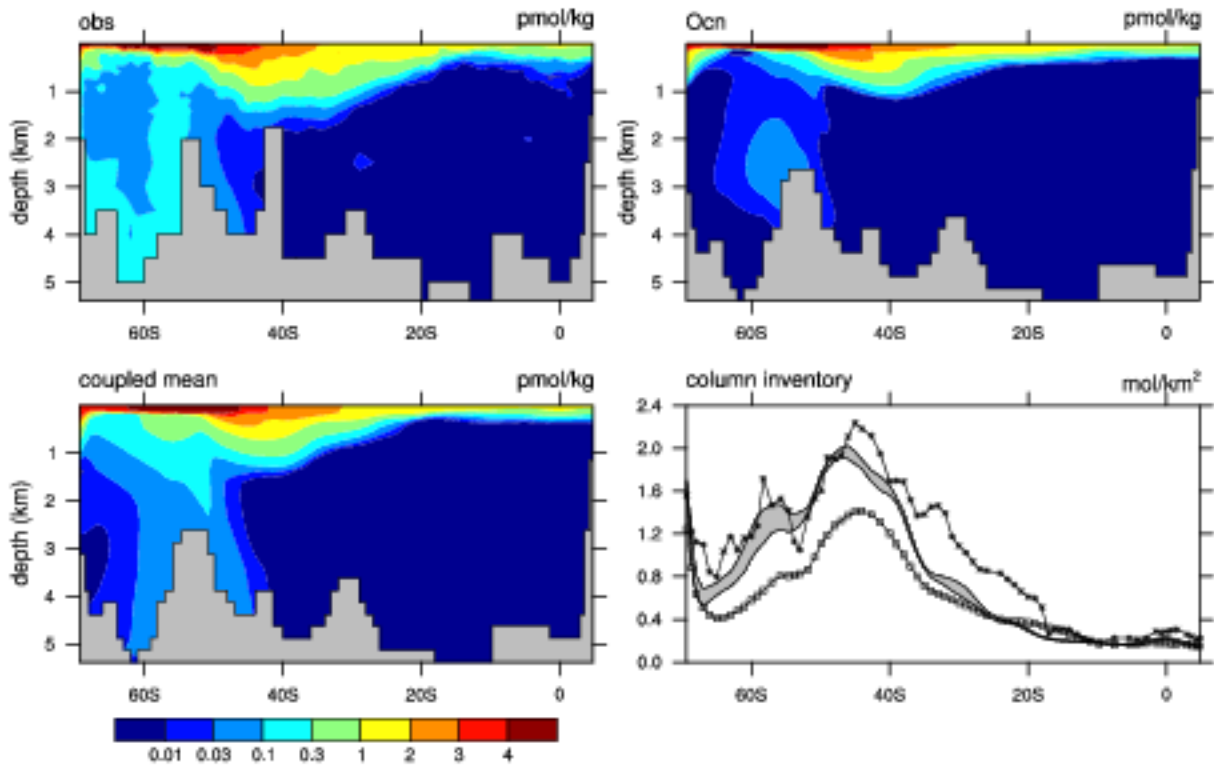
CFC 11, na93, 1993-08

Figure 1. CFC-11 from the na93 section along 20°W taken in August 1993. (a) Observations, (b) ocean alone Ocn run, (c) mean of the ESb, ESg and ESh runs, and (d) column inventory of CFC-11 in moles km^{-2} along the section from observations (crosses), Ocn run (squares), and the range of the ESb, ESg and ESh runs (shading).

Figure 2. Same as Fig. 1, but from the WOCE ajax section along 0°taken in October 1983.
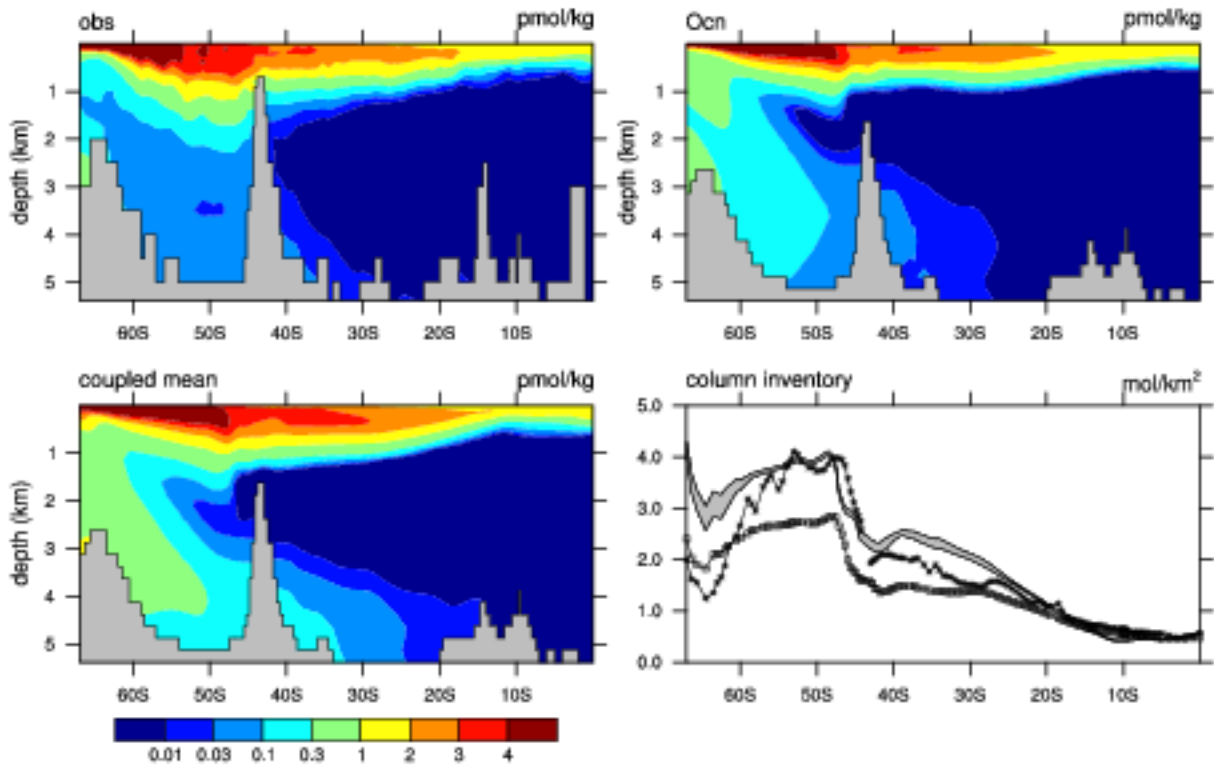
Figure 3. Same as Fig. 1, but from the WOCE p14s section near 170°E taken in February 1996.
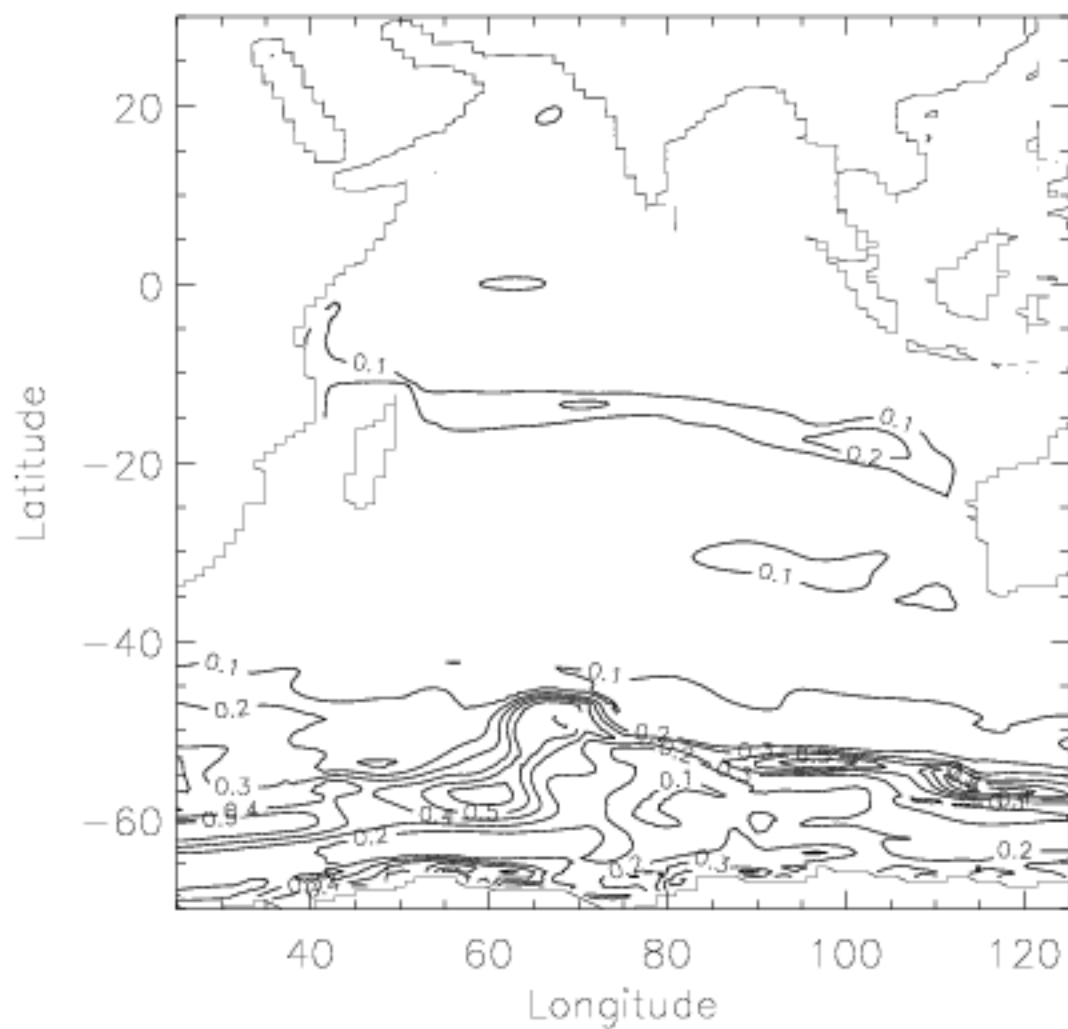
Figure 4. The rms of CFC-11 relative to the ensemble mean annual cycle over 1995 at 200 m depth in the Indian Ocean using the ESb, ESg and ESh runs; CI is 0.1 pmoles kg^{-1}.
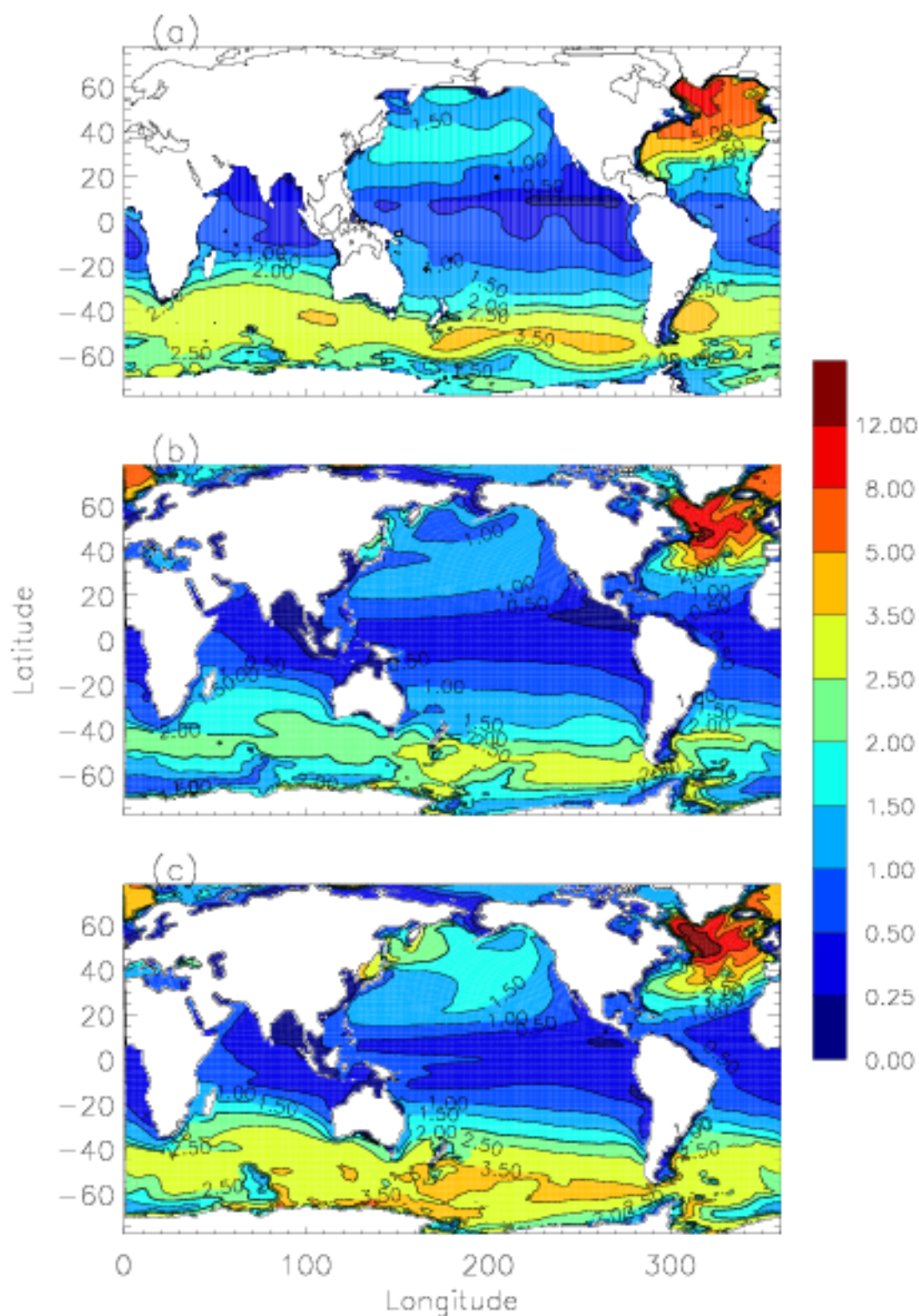
Figure 5. Column inventory of CFC-11 in moles km^{-2} for 1994. (a) WOCE data from Willey et al. (2004), (b) ocean alone Ocn run, and (c) mean of ESb, ESg, and ESh runs.

22
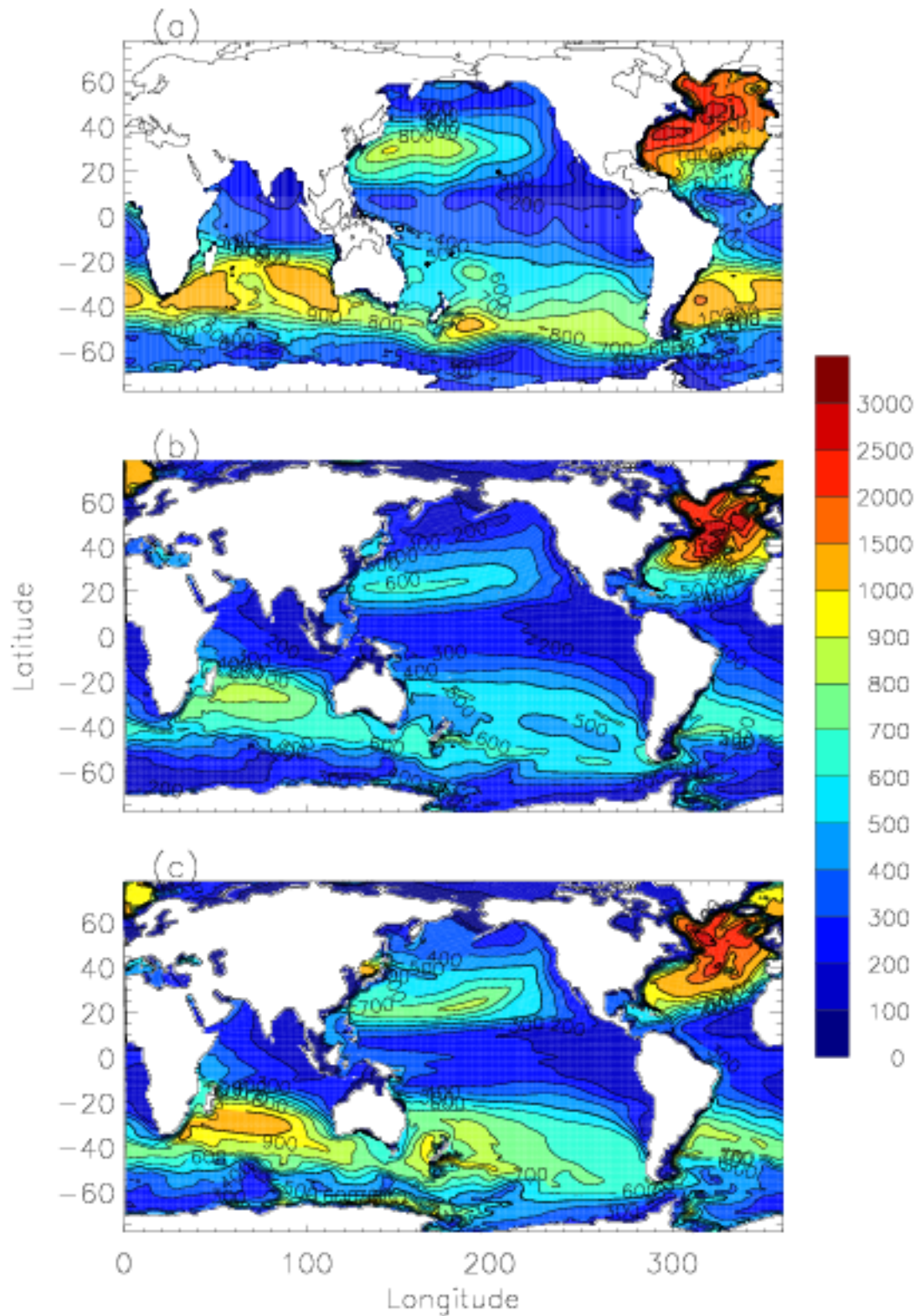
Figure 6. Same as Fig. 5, but for penetration depth in m.
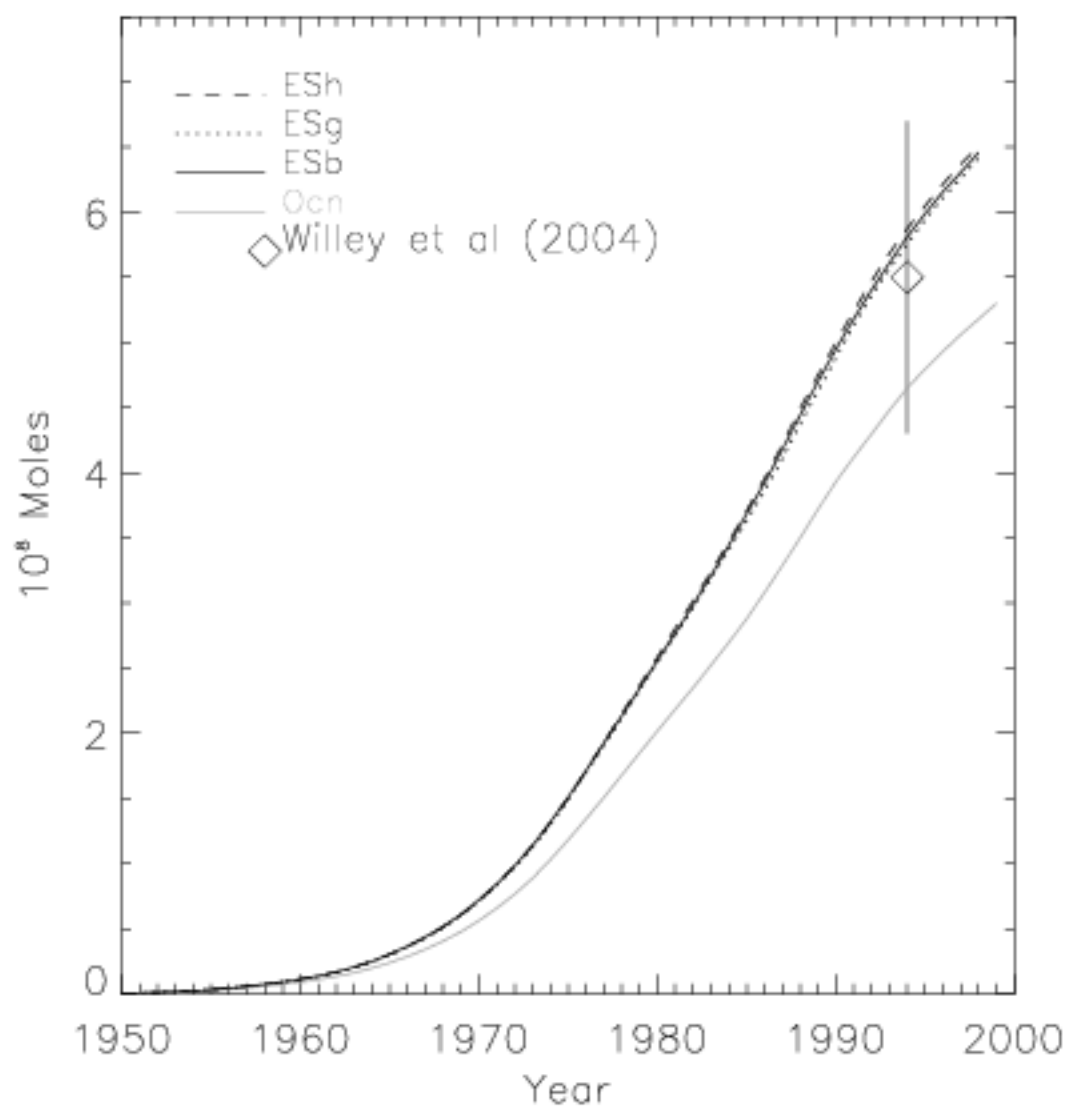
Figure 7. Time series of the global inventory of CFC-11 in moles from the ESb, ESg, ESh, and Ocn runs. Also plotted is the Willey et al. (2004) estimate centered on 1994.
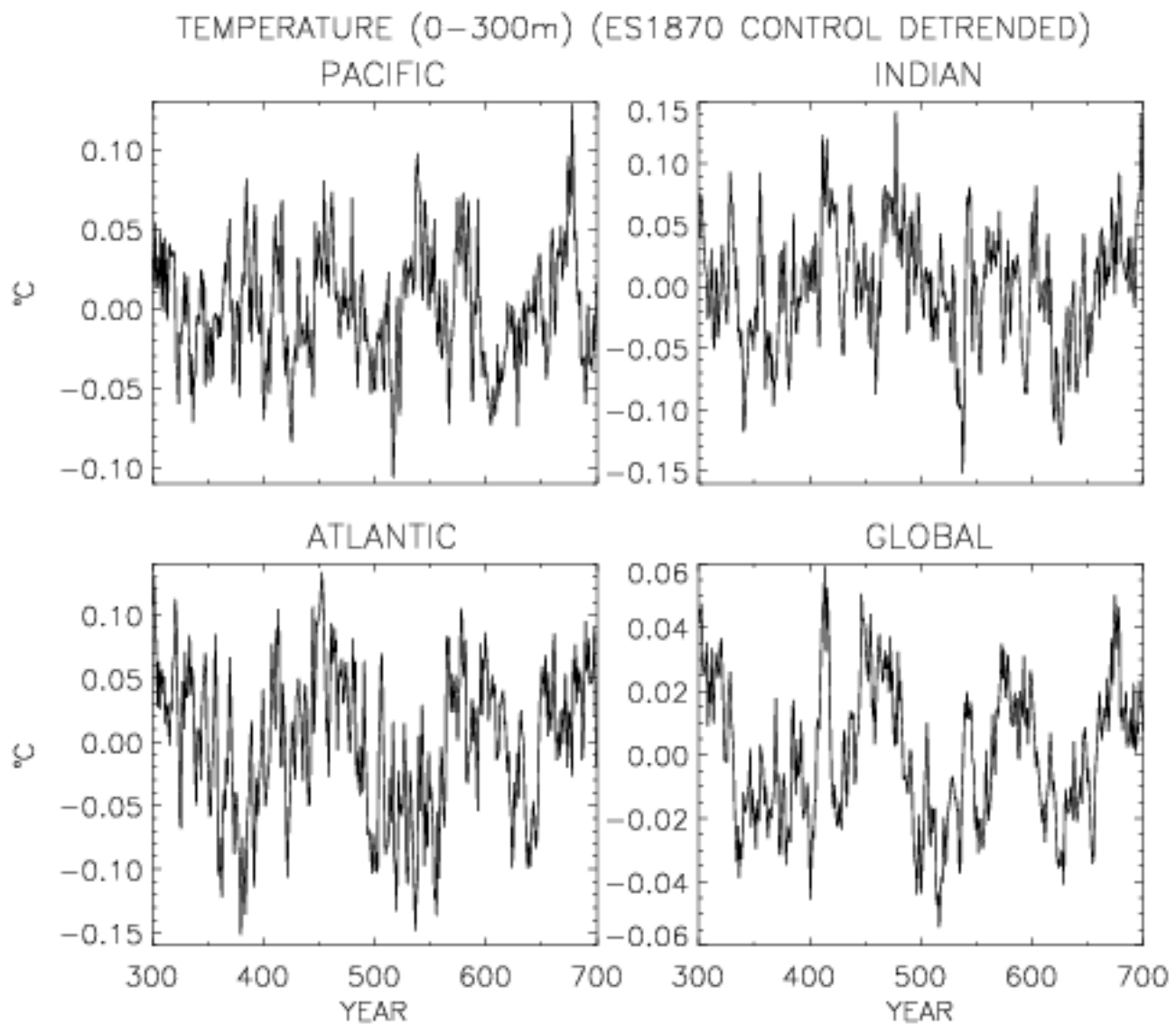
Figure 8. Detrended time series of the 300 m average temperature anomaly in °C from the ES1870 control run. (a) Pacific Ocean, (b) Indian Ocean, (c) Atlantic Ocean, and (d) Global Ocean.

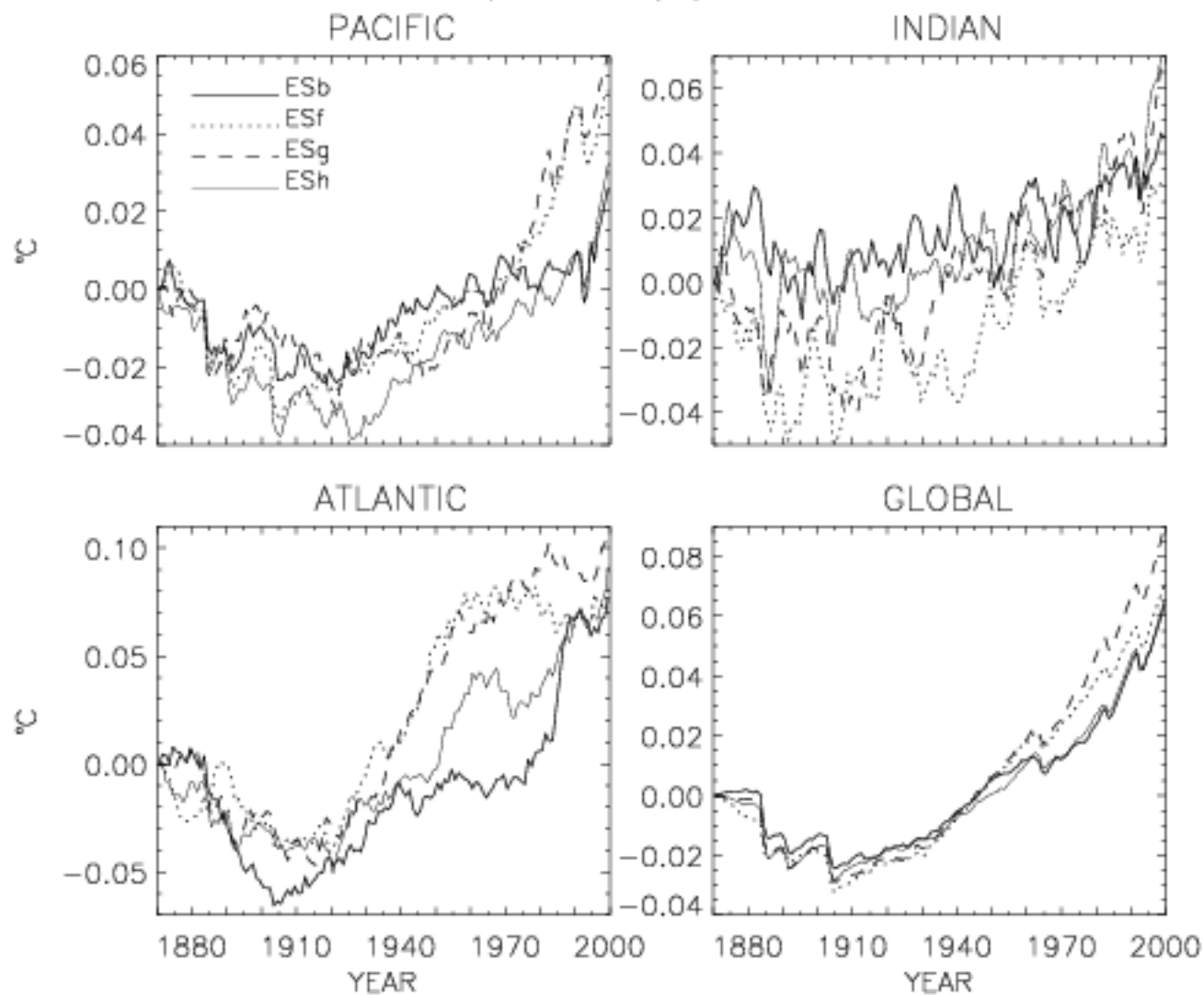TEMPERATURE DIFFERENCE (0−300m) (20TH CEN. − ES1870 CONTROL)
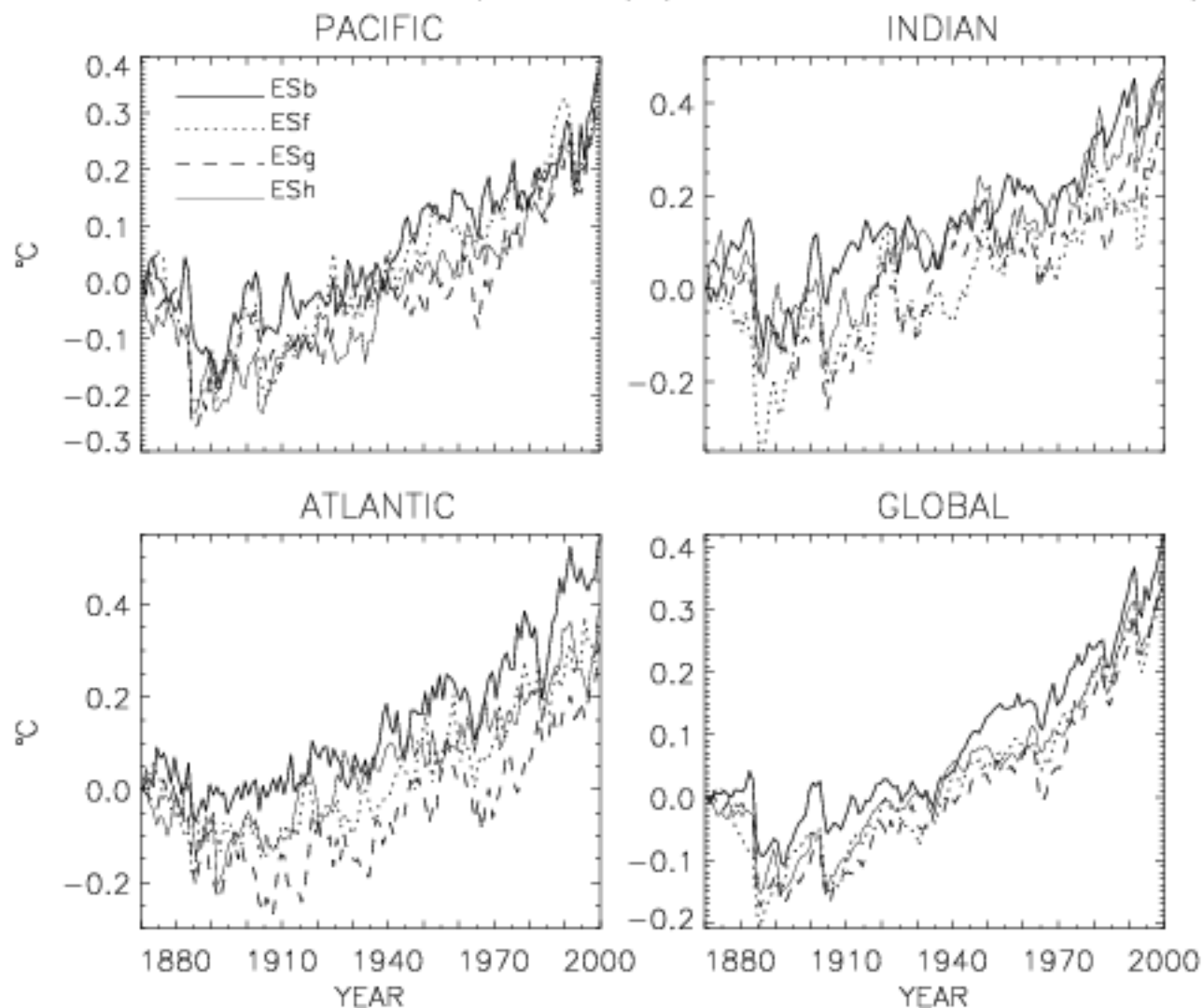
Figure 9. Time series of the 300 m average temperature difference in °C between the ESb, ESf, ESg and ESh runs minus the ES1870 control run. (a) Pacific Ocean, (b) Indian Ocean, (c) Atlantic Ocean, and (d) Global Ocean.
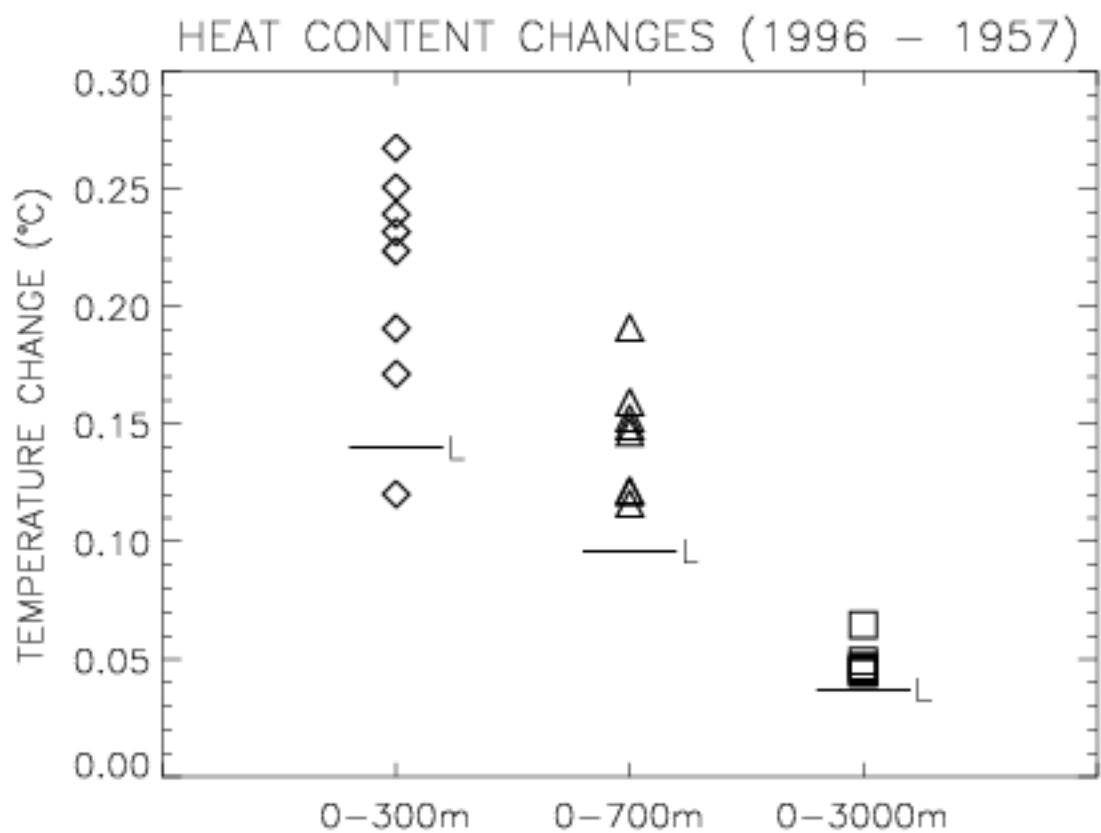
26

Figure 10. Same as Fig. 9, but for the 3 km average temperature.

Figure 11. The 300 m, 700 m and 3 km average temperature increases in °C for the Global Ocean between 1957 and 1996 from the ensemble of 20th Century runs. Also plotted are the Levitus et al. (2005) observational estimates.
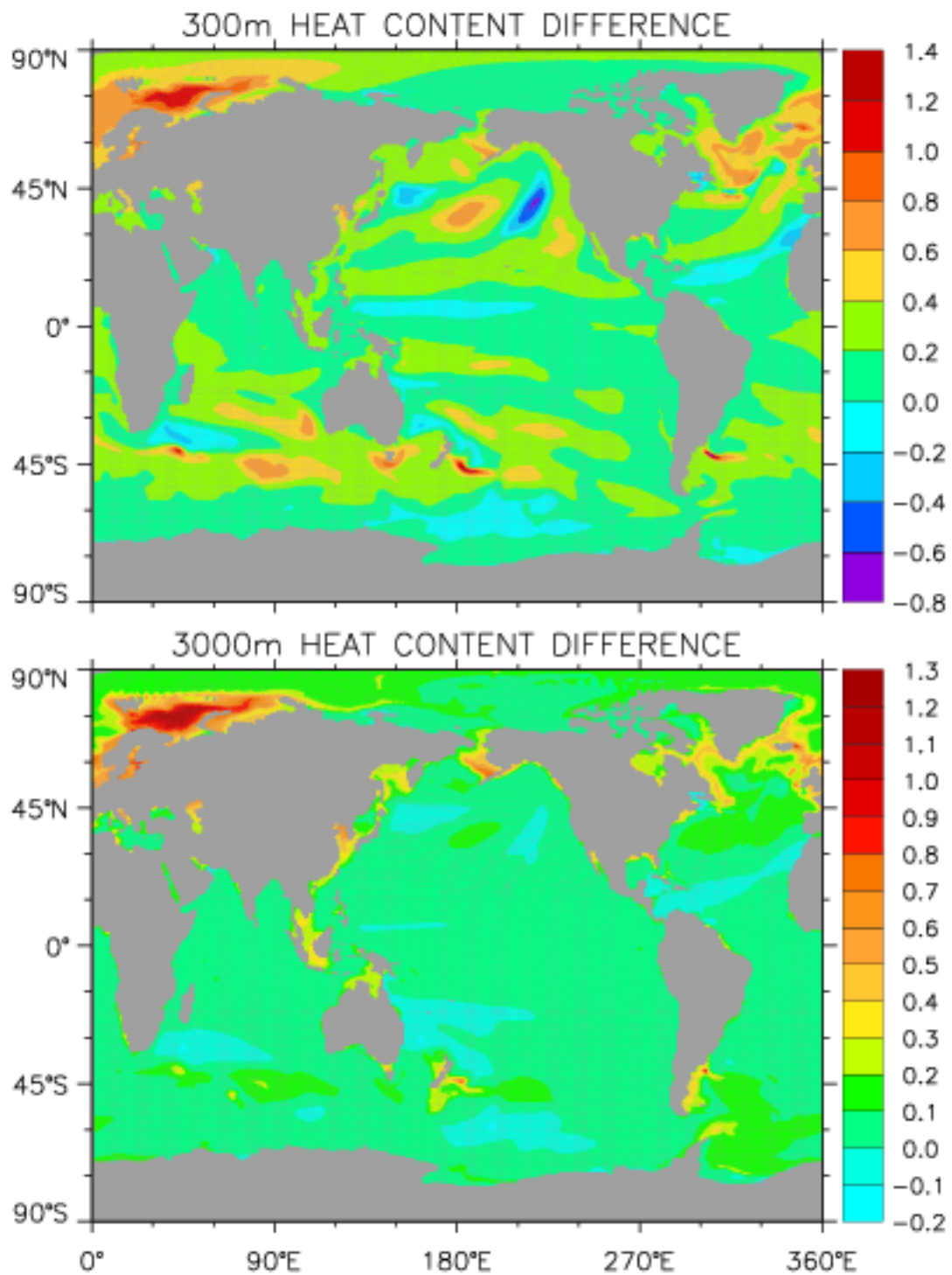
Figure 12. The ensemble mean 20th Century average temperature change between 1955-1959 and 1994-1998 in °C: a) 300 m and b) 3 km.
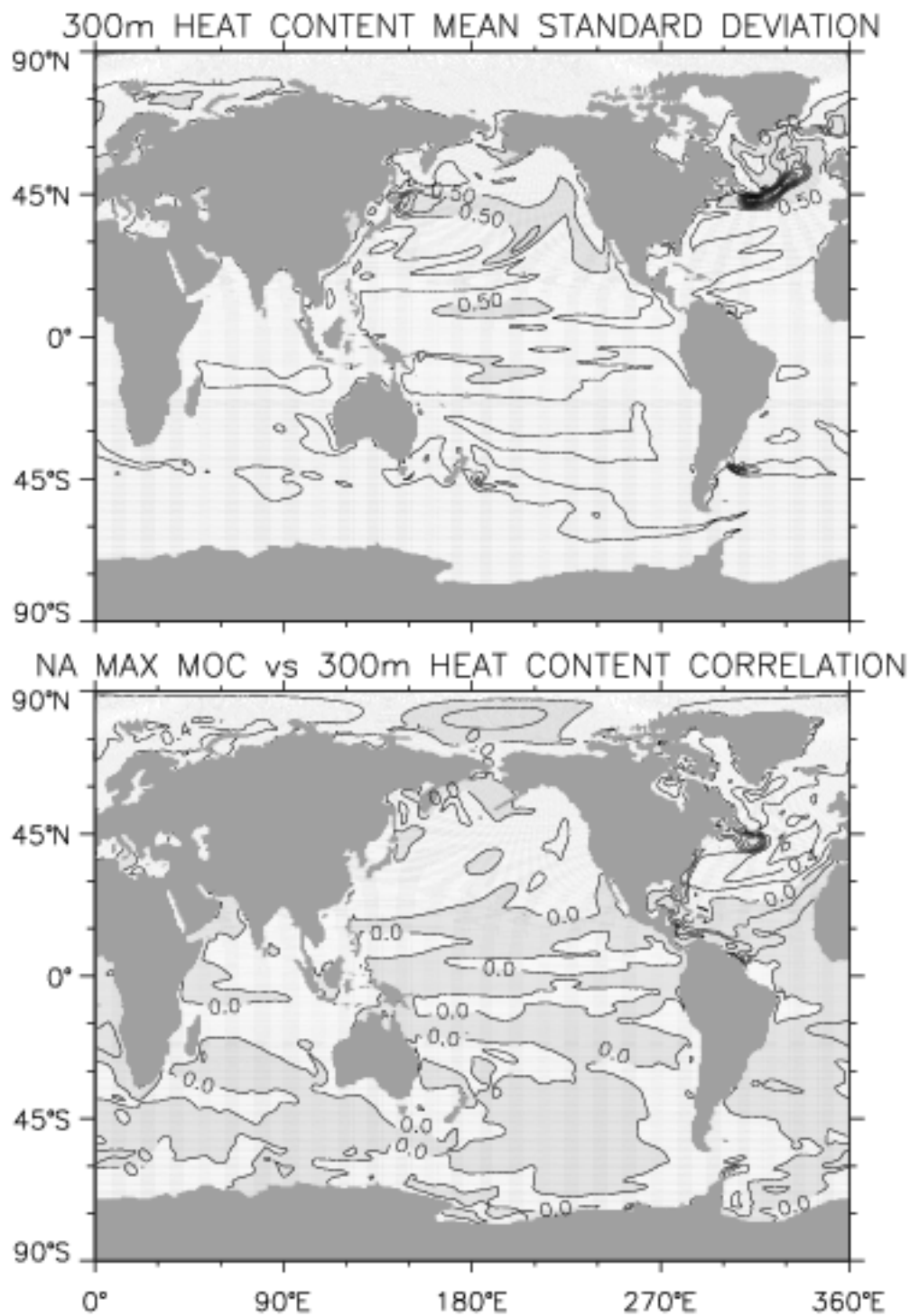
Figure 13. Standard deviation of the 300 m heat content among the 20th Century ensemble; CI is 0.25°C, and b) correlation between the North Atlantic meridional overturning maximum and the 300 m heat content over years 300-700 from the ES1870 control run; CI is 0.2.